HIPPOCAMPUS 22:1164–1175 (2012)

Theta and Gamma Coherence Across the Septotemporal Axis During Distinct Behavioral States

Stephanie C. Penley,[1] James R. Hinman,[1] Helen R. Sabolek,[1] Monty A. Escabí,[1,2,3] Etan J. Markus,[1] and James J. Chrobak[1]*

ABSTRACT: Theta (4–12 Hz) and gamma (40–100 Hz) field potentials represent the interaction of synchronized synaptic input onto distinct neuronal populations within the hippocampal formation. Theta is quite prominent during exploratory activity, locomotion, and REM sleep. Although it is generally acknowledged that theta is coherent throughout most of the hippocampus, there is significant variability in theta, as well as gamma, coherence across lamina at any particular septotemporal level of the hippocampus. Larger differences in theta coherence are observed across the septotemporal (long) axis. We have reported that during REM sleep there is a decrease in theta coherence across the long axis that varies with the topography of CA3/mossy cell input rather than the topography of the prominent entorhinal input. On the basis of differences in the rat's behavior as well as the activity of neuromodulatory inputs (e.g., noradrenergic and serotonergic), we hypothesized that theta coherence across the long axis would be greater during locomotion than REM sleep and exhibit a pattern more consistent with the topography of entorhinal inputs. We examined theta and gamma coherence indices at different septotemporal and laminar sites during distinct theta states: locomotion during maze running, REM sleep, following acute treatment with a θ-inducing cholinomimetic (physostigmine) and for comparison during slow-wave sleep. The results demonstrate a generally consistent pattern of theta and gamma coherence across the septotemporal axis of the hippocampus that is quite indifferent to sensory input and overt behavior. These results are discussed with regards to the neurobiological mechanisms that generate theta and gamma and the growing body of evidence linking theta and gamma indices to memory and other cognitive functions. © 2011 Wiley Periodicals, Inc.

KEY WORDS: hippocampus; REM; entorhinal cortex; memory; septotemporal

INTRODUCTION

Rhythmic field potentials such as theta and gamma reflect neurobiological clocking mechanisms for bringing spatially distributed cell assemblies together in time, as well as isolating or temporally differentiating cell assemblies (Llinas et al., 1991; Gray, 1994; Buzsaki and Chrobak, 1995; Csicsvari et al., 2003; Llinas et al., 2005). The dynamic synchronization and temporal isolation of neuronal ensembles is likely a key feature of brain function. Our laboratory has been exploring the synchronization (coherence) of theta and gamma field potentials across the septotemporal axis of the hippocampus in an attempt to understand the conditions that may promote unitary activity vs. conditions that may isolate septotemporal areas of the hippocampus (HPC). Such information may contribute to our understanding of functional differentiation along the septotemporal axis (e.g., Moser and Moser, 1998; Bannerman et al., 2004).

Theta (4–12 Hz) and gamma (40–100 Hz) field potentials within the hippocampal formation [HPC and entorhinal cortex (EC)] represent the interaction of synchronized synaptic inputs, both excitatory and inhibitory, onto the laminarly organized somatodendritic field of hippocampal pyramidal, granule, and GABAergic neurons (Buzsaki et al., 1983; Brankack et al., 1993) Several key circuit elements contribute to theta and gamma current generation (e.g., amplitude of LFPs) and coherence across sites including minimally: (1) excitatory (glutamatergic) hippocampal neurons (dentate granule cells, hilar mossy cells, CA3, and CA1 pyramidal neurons); (2) excitatory entorhinal cortical inputs from Layers 2–3 neurons (Alonso and Garcia-Austt, 1987; Chrobak and Buzsaki, 1998); (3) networks of categorically distinct GABAergic neurons (e.g., basket cells, subclasses of dendritic-targeting cells; Konopacki et al., 1992; Ylinen et al., 1995; Hajos et al., 2004); (4) medial septal cholinergic inputs, as well as several subcortical neuromodulatory inputs (e.g., serotonergic, noradrenergic, histaminergic; Brazhnik and Fox, 1999; see Vertes and Kocsis, 1997 for review); (5) medial septal GABAergic neurons that selectively target specific subpopulations of hippocampal GABAergic neurons (Freund and Antal, 1988; Borhegyi et al., 2004, Hangya et al., 2009); and (6) GABAergic hippocampo-septal neurons that feedback to the medial septal GABAergic neurons (Toth et al., 1993; Manseau et al., 2008).

These diverse elements are responsible for a remarkably well-synchronized product that manifests in a laminar specific profile of theta and gamma field potentials (Bullock et al., 1990; Bragin et al., 1995) and the phase-related discharge of most hippocampal

[1] **Department of Psychology, University of Connecticut, Storrs, Connecticut;** [2] **Department of Biomedical Engineering, University of Connecticut, Storrs, Connecticut;** [3] **Department of Electrical and Computer Engineering, University of Connecticut, Storrs, Connecticut**
Grant sponsor: NSF; Grant number: 0919783
*Correspondence to: James J Chrobak, Department of Psychology, University of Connecticut, Storrs, CT 06269. E-mail: james.chrobak@uconn.edu
Accepted for publication 4 April 2011
DOI 10.1002/hipo.20962
Published online 11 July 2011 in Wiley Online Library (wileyonlinelibrary.com).

neurons (Leung and Buzsaki, 1983; Leung, 1984; Bland, 1986; O'Keefe and Reece, 1993). Theta signals across sites within the HPC and between the HPC and EC are fairly coherent (Buzsaki, 2002), despite widespread topographic variation in intrinsic (associational and commissural) hippocampal afferents, entorhinal afferents and subcortical afferents (Amaral and Kurz, 1985; Amaral and Witter, 1995, Dolorfo and Amaral, 1998). While a number of studies have examined the local variation in theta (and gamma) within sites of the septal HPC, few studies have examined coherence across the septotemporal axis (although see Bullock et al., 1995; Sabolek et al., 2009; Royer et al., 2010).

We are interested in understanding the role of theta coherence along the septotemporal (areal or long) axis, its relation to the topography of entorhinal afferents (Dolorfo and Amaral, 1998) and the conditions that may alter theta or gamma coherence. During REM sleep there is a significant decrease in theta coherence across the long axis (Sabolek et al., 2009). In contrast, theta coherence across hemispheres is quite high between homotypic sites (left septal DG to right septal DG; Kocsis et al., 1994; Sabolek et al., 2009). These findings demonstrate that theta coherence is not varying as a function of distance per se but rather in relation to anatomical connectivity. Given the prominent intrahemispheric (commissural) CA3/mossy cell projection and the unilateral nature of the EC input, these findings also demonstrate that during REM, theta coherence across the septotemporal axis varies largely in relation to the topography of intrahippocampal CA3/mossy cell projections.

Theta and gamma rhythms are generated in the hippocampal formation during distinct behavioral states including REM sleep, exploratory activity and locomotion, as well as during awake-immobility in association with the administration of cholinomimetics (e.g., physostigmine; see Lee et al., 1994). Although each of these behavioral states is correlated to the theta rhythm, few studies have defined fundamental differences in the character of the theta signal during these distinct theta states. There is a sharp decrease in the discharge of locus coeruleus and raphe neurons during theta associated with REM sleep and a corresponding decrease in norepinephrine (NE) and serotonin (5-HT) levels during REM as compared with the awake state (Aston-Jones and Bloom, 1981; Trulson and Trulson, 1982). While theta rhythmicity is evident in the absence of NE and 5-HT input, acetylcholine (ACh) (Ach) input primarily from medial septal neurons plays an important role in the generation of theta. Cholinergic antagonists suppress theta, while the administration of cholinomimetics typically enhance theta and can induce theta even in the absence of locomotor activity (Kramis et al., 1975; Leung and Vanderwolf, 1980; Bland, 1986). Thus following sufficient physostigmine treatment, rats will sit relatively immobile while exhibiting sustained bouts of theta activity in hippocampus. Theta in the absence of locomotion led Vanderwolf and coworkers to suggest the existence of an atropine-sensitive theta (cholinergic component) and atropine-insensitive component coexistent during active exploration (see Bland and Oddie, 2001 and Lee et al., 1995 and for extensive discussion). In contrast to the decrease in NE and 5-HT levels during REM sleep, ACh levels have been reported to be as high or higher than the awake state in both rats and cats (Kametani and Kawamura, 1990; Marrosu et al., 1995). While theta field potentials largely represent synchronized excitatory (glutamatergic) and inhibitory (GABAergic), onto the somato-dendritic field of hippocampal neurons, neuromodulatory inputs (e.g., NE, 5-HT and Ach) enhance and suppress the relative efficacy of both glutamatergic and GABAergic inputs impinging on CA3, CA1 and dentate neurons (see Hasselmo, 2006, Harley, 2007 as well as Sil'kis, 2009 for reviews and discussion). Does the net effect of behavior differences (e.g., running, immobile, asleep) and/or neuromodulatory differences alter the coherence of the theta signal across the septotemporal axis of the hippocampus?

This study examined variability in theta and gamma indices within the HPC during distinct states: REM, locomotion during maze running, following acute treatment with a θ-inducing cholinomimetic (physostigmine) and for comparison during slow-wave sleeo, Despite dramatic behavioral differences (locomotion across a linear track, general immobility and unconscious behavior associated with REM sleep, and awake and upright, immobility associated with physostigmine-treatment), we demonstrate a consistent pattern of theta coherence across the septotemporal axis of the HPC.

MATERIALS AND METHODS

Animals and Surgeries

Seven adult male rats (Fisher-344) were used in this study. The animals were housed on a 12-h/12-h light-dark cycle, in a temperature-controlled room. All procedures were performed in accordance with the guidelines set forth by University of Connecticut's Institutional Animal Care and Use Committee and NIH.

Rats were anesthetized with a ketamine cocktail (4 ml/kg) consisting of (in mg/ml): 25 ketamine, 1.3 xylazine, and 0.25 acepromazine. After a midline scalp incision, four holes were drilled in the skull over the HPC and four electrode arrays were positioned along the septo-temporal extent of the HPC. All electrodes were attached to female pins (Omnetics, Minneapolis, MN) secured in a rectangular five by four pin array. Two stainless steel watch screws driven into the skull above the cerebellum served as indifferent and ground electrodes. Two or more additional support screws were positioned over the anterior aspect of the skull and the entire ensemble was secured with dental acrylic.

The majority of electrodes were targeted to sites below the hippocampal fissure to include positions in stratum moleculare (molecular layer), the granule cell layer and the hilus of the DG (see Figs. 1A,B). Each septal electrode array consisted of four linearly spaced 50 μm tungsten wires (16 total electrodes; California Fine Wire Co., Grover Beach, CA). Each wire was threaded into one of four adjacent pieces of fused silica tubing (180 μm outer diameter; Polymicro Tubing, Phoenix, AZ).

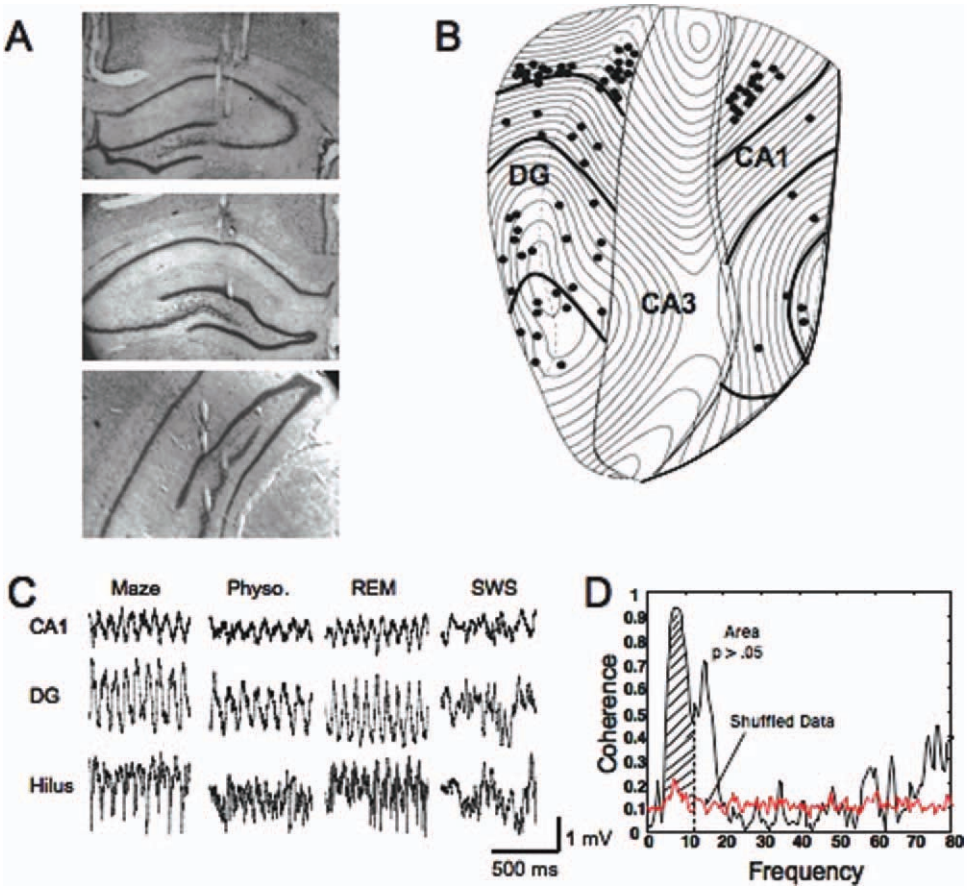

FIGURE 1. Electrode positions along the septo-temporal axis of the hippocampus. A: Photomicrograph showing tracts from electrode arrays positioned at three septotemporal positions of the DG, CA1, and hilus. B: Flat map representations of the DG, CA3, and CA1 subfields (adapted from Swanson and Cowan, 1978). The position of each electrode was plotted on a flatmap of the DG or CA1 using the approximate distance measured in millimeters from the septal pole. Each contour line represents 180 μm of tissue through coronal sections. C: Concurrent recordings from DG, CA1, and hilus illustrating the laminar profile of theta and gamma oscillations. Note the prominent theta oscillations and phase reversal present in the CA1 and DG traces, as well as the prominent gamma oscillations in the hilus. D: Coherence as a function of frequency (black line). A normalized coherence value was calculated as the area above the 95% confidence interval of shuffled signals (red line) for each electrode pair exhibiting theta peaks between 6 and 10 Hz. [Color figure can be viewed in the online issue, which is available at wileyonlinelibrary.com.]

Each septal array (four pieces of silica tubing each with a threaded wire) had a rough size of 180 μm thick and 720 μm wide with spacing of roughly 180 microns between electrode wires. The septal electrodes were then cut at roughly a 45° angle which allowed them to span approximately 1 mm dorsoventrally targeting different laminar positions from the dorsal aspect of stratum radiatum thru to the hilar region (see illustration in Fig. 4 of Sabolek et al., 2009). Electrode arrays positioned at more temporal sites were more widely spaced with electrode wires positioned in alternate tubes of seven adjacent pieces of silica tubing (180 μm thick and 1,260 μm wide) and not cut at an angle as laminar fields becomes oriented in mediolateral dimension. Typically three arrays were positioned into one hemisphere of the HPC at distinct septotemporal locations, and the fourth array was positioned in the contralateral septal HPC. The targeted positions included arrays at the following coordinates (relative to bregma): AP: −2.5, −5.5, −7.5 mm; ML: 2.2, 5.0, 6.0; DV, 3.0–7.0 mm.

Electrophysiological Recordings and Data Analysis

Details of the electrophysiologic recording and analysis procedures have been described elsewhere (Sabolek et al., 2009). Wide-band electrical activity was recorded (1–2,000 Hz, 4,006 samples/s) using a Neuralynx data acquisition system (Tucson, AZ). Electrophysiological recordings occurred during the light phase of the light/dark cycle. Recordings were made while rats foraged for food on a twelve arm radial maze, during REM and slow wave sleep (SWS) sleep, and after treatment with physostigmine (1.0 mg/kg, i.p). REM recordings were collected in the animals' home cage. Recordings commenced once the rat engaged in a sleeping posture, typically curled up with eyes closed, and theta activity was present. All REM bouts were defined by both the absence of any movement, as well as a relaxed "sleeping" posture, and were preceded by large irregular EEG (SWS) activity. SWS data was selected from an episode

TABLE 1.

Theta/Delta Power Ratio

	CA1	DG	Hilus
Theta/Delta	(N = 22)	(N = 26)	(N = 33)
Maze running	1.29 ± 0.02	1.29 ± 0.03	1.03 ± 0.01
REM	1.33 ± 0.02	1.29 ± 0.03	1.06 ± 0.01
Physostigmine	1.13 ± 0.02	1.15 ± 0.02	1.01 ± 0.01
SWS	0.91 ± 0.00	0.93 ± 0.01	0.94 ± 0.00

All values expressed as dB relative to 1 μV in theta band (6–10 Hz) divided by dB relative to 1 μV across delta band (1–4 Hz).

preceding REM by no more then 10 min. SWS epochs were defined by the presence of large irregular waves in the EEG as well as a decrease in theta/delta ratio (see Table 1). The entire duration of each REM episode (typically lasting 30 s–2 min) was collected, and data selection (Adobe Audition 1.0) and analyses (Matlab, Mathworks Inc, Natick, MA) were performed off-line.

A total of thirty seconds of data were used for analysis from each behavioral state (maze running, REM, physostigmine-induced theta and SWS). The EEG traces were visually scanned (Adobe Audition 1.0) and three-second epochs of artifact free theta activity with peak frequencies of 6–8 Hz were selected for each channel. Ten of these nonoverlapping three-second epochs were then concatenated to produce a total of 30 s of continuous EEG data for analysis of both power spectral density and coherence. The same 30 s of data was used for both analyses. Power spectral density estimates were then obtained in Matlab using Welch's averaged modified periodogram method (Welch, 1967). Power values across behavioral states were analyzed as a function of laminar position using repeated measures ANOVAs, followed by Tukey HSD tests or paired *t*-tests.

Coherence values (Bullock et al., 1990) for each channel pair were computed using the Welch periodogram estimation procedure with a spectral resolution of ~2 Hz. Coherence is a measure of the linear association between two signals as a function of frequency. As such, two signals can differ in either amplitude and/or phase and still be highly coherent assuming the relationship between the amplitude and/or phase of the two signals remains constant. To ensure that the measured coherence values were not due to chance alone, a significance estimation procedure was devised in which the coherence estimate for a pair of electrodes was compared against a null hypothesis condition consisting of signals with identical magnitude spectrum, but with zero phase coherence (Sabolek et al., 2009, Hinman et al., 2011; Fig. 1D). For each channel pair, the cumulative distribution of frequency-dependent coherence values were created by randomizing the phase spectrum of both signals (Efron and Tibshirani, 1993). This was accomplished by circularly phase shifting one signal in the pair by a random amount (preserving the magnitude spectrum), and calculating the coherence for the random phase signals. This procedure was then bootstrapped 250 times. This procedure guarantees that the signal spectrums are identical, but have no linear association because the phase or time information has been removed. The coherence distribution for this null (random phase) condition was used to determine a significance threshold for each frequency band (2 Hz resolution), below which 95% of the shifted null hypothesis coherence values fell (see also Fig. 1D). Thus, only regions of the nonshuffled signal coherences falling above the 95% threshold were considered significant. For each channel pair, the mean coherence values for statistically significant frequencies in the theta (6–10 Hz) and gamma (40–100 Hz) band were calculated (expressed as average coherence value per Hz). Average coherence values were normalized relative to the observed maximum for each frequency range, determined by calculating the significant area in each frequency range for a channel pair where both elements of the pair are the same channel (C_{xx} = 1.0 at all frequencies). The resulting normalized coherence value falls between 0 and 1. The standard theta coherence (non-normalized) for each homotopic channel pair was also calculated (see Table 2), and a correlation was run between the normalized and standard coherence values. All coherence values were calculated between electrode pairs located within homotopic laminar positions (same laminar subfield e.g., stratum moleculare and stratum moleculare at a different septotemporal locations) ipsilaterally and homotypic positions contralaterally (same laminar subfield), unless otherwise indicated. Normalized coherence values for each channel pair were then analyzed as a

TABLE 2.

Non-normalized Theta Coherence by Distance

	CA1-CA1	DG-DG	Hilus-Hilus
	(n = 4)	(n = 10)	(n = 5)
Within hemisphere first septal quartile			
Maze running	0.94 ± 0.01	0.88 ± 0.02	0.74 ± 0.07
REM	0.92 ± 0.03	0.83 ± 0.04	0.73 ± 0.14
Physostigmine	0.90 ± 0.03	0.79 ± 0.06	0.73 ± 0.08
SWS	0.56 ± 0.08	0.63 ± 0.08	0.61 ± 0.05
Within hemisphere first to second quartile			
	(n = 5)	(n = 7)	(n = 17)
Maze running	0.71 ± 0.08	0.68 ± 0.07	0.61 ± 0.04
REM	0.75 ± 0.05	0.67 ± 0.04	0.54 ± 0.04
Physostigmine	0.60 ± 0.05	0.53 ± 0.07	0.50 ± 0.03
SWS	0.41 ± 0.07	0.38 ± 0.06	0.47 ± 0.05
Within hemisphere first to third quartile			
	(n = 1)	(n = 4)	(n = 8)
Maze running	0.52 ± N/A	0.43 ± 0.12	0.41 ± 0.04
REM	0.53 ± N/A	0.50 ± 0.04	0.44 ± 0.05
Physostigmine	0.53 ± N/A	0.28 ± 0.03	0.36 ± 0.02
SWS	0.34 ± N/A	0.29 ± 0.03	0.29 ± 0.01

All values expressed as standard coherence ± SEM. Values are averaged across homotopic (e.g., CA1-CA1) and septo-temporal positions. N = number of homotopic electrode pairs. The correlation between normalized and standard coherence was r = 0.99 for REM, r = 0.98 for the maze condition, r = 0.97 following physostigmine treatment, and r = 0.98 during SWS.

function of laminar position of electrodes and the distance between each electrode pair, using repeated measures ANOVAs followed by Tukey HSD tests or paired *t*-tests.

In addition to coherence of either theta and gamma across electrode sites, the cross frequency coupling of theta and gamma at single electrode sites was assessed using a procedure similar to that employed by Hentschke et al. (2007). Signals from a single electrode site were bandpass filtered for theta (4–16 Hz) and gamma (40–100 Hz) and then the envelope of the gamma signal was obtained by taking the magnitude of the Hilbert transform of the gamma signal. Coherence between the theta signal and the envelope of the gamma signal was then calculated (as described above). As with the coherence between electrode sites, coherence between the theta signal and the envelope of the gamma signal at a single electrode site was computed using the Welch periodogram estimation procedure with a spectral resolution of ~2 Hz and the same significance estimate procedure (as described above) was also used to determine the cross frequency coupling between theta and gamma above a 95% significance threshold.

Histology

Following the completion of recording, rats were anesthetized with Euthasol (390 mg/kg sodium pentobarbital and 50 mg/kg phenytoin solution) and transcardially perfused with ice-cold saline followed by 4% paraformaldehyde in 0.1M phosphate buffer (pH 7.2). Brains were sliced (50 μm sections) using a vibratome (Vibratome Series 1,500), mounted, and Nissl stained using thionin. All electrode positions were verified and categorized according to laminar and septotemporal position. Septotemporal distances between electrode positions were determined by noting the location of each electrode position on a flat-map representation of the HPC (Swanson, 1978). Each section of a flatmap represents ~180 μm of tissue, and so fairly accurate approximations of the relative distance between electrodes could be determined by counting the number of sections between two electrodes. Photomicrographs of relevant electrode tracks were captured using a Nikon microscope connected to a Spot RT camera system, digitized and prepared for presentation using Adobe Photoshop 7.0.

RESULTS

The majority of electrodes sites were located just below the hippocampal fissure in the dentate gyrus (DG); including positions in the dendritic field of the granule cells (stratum moleculare), the granule cell layer and within the hilus ($N = 59$ sites; see Fig. 1A). In addition, 22 electrode sites were located in the CA1 region with most in stratum oriens or pyramidale (see Fig. 1A). The position of electrode sites along the septotemporal axis is plotted on a flatmap representation of the HPC (Swanson, 1978) where contour lines represent coronal sections (see Fig. 1B).

Theta and Gamma Power Across Different Behavioral States

Theta oscillations (0.2–1.0 mV) were observed visually, as well as in spectrograms, in all electrode sites sampled during maze running, REM sleep and physostigmine treatment (see Figs. 1C and 2A). The relative amplitude (ratio of total power between 1 and 100 Hz) of theta signals was largest nearest the hippocampal fissure at sites within stratum moleculare of DG (see Fig. 1C and Table 3). Signals at CA1 sites exhibited similar power during all theta states, but were phase-shifted as compared with dentate and hilar sites. The laminar profile of theta power and phase-shifts across CA1, DG, and hilar sites were similar across the septotemporal axis, as well as across distinct theta states (maze running, REM, and physostigmine-induced). Theta power was reduced (CA1, DG, and hilar) sites during physostigmine-induced theta as compared to theta power during maze running and REM ($P < 0.001$; see Fig. 2A and Table 3).

Gamma (40–100 Hz) power was significantly different across laminar positions. Gamma signals at hilar sites had significantly greater gamma power than signals at DG or CA1 sites ($P < 0.001$; see Figs. 2C and 3B and Table 3) during all theta states, as well as during SWS. Gamma signals in DG also exhibited higher gamma power compared to CA1 sites across all theta states ($P < 0.001$; see Figs. 2C and 3B and Table 3). Gamma power was increased across CA1 and DG sites during physostigmine-induced theta as compared with gamma power during maze running and REM ($P < 0.01$; see Table 3). The increase in CA1 and DG gamma during physostigmine was often related to a clear peak in gamma power near 40 Hz and an obvious shift toward lower frequency gamma (see Fig. 2B) particularly at electrode sites deep in stratum radiatum or nearest the hippocampal fissure. Lastly, gamma power was reduced at all sites during SWS as compared with gamma power during maze running and REM ($P < 0.001$; see Fig. 2B, Table 3).

Theta Coherence Across the Septotemporal Axis

Coherence of theta was calculated using a statistical thresholding procedure in which normalized coherence values represent the area within a specific frequency band that falls above the 95% confidence interval created by randomly shuffling the signal phase spectrum in the time domain. To simplify the analysis across the septotemporal axis, the hippocampal electrode sites were binned into quartiles (see Fig. 3A). Thus, theta coherence was measured between homotopic locations either within the "first" or septal most quartile (e.g., a–b sites in Fig. 3A), across hemispheres within the septal most quartiles (e.g., a–c sites in Fig. 3A), across the first and second quartiles (e.g., a–d sites in Fig. 3A), or across the first and third quartiles (e.g., a–e sites in Fig. 3A). The standard coherence was also calculated for each homotopic channel pair (see Table 2). The average difference between the standard coherence and normalized coherence ranged from an increase of approximately 0.2 for the SWS conditions to between a 0.02–0.04 increase for the REM, maze and physostigmine conditions (regardless of

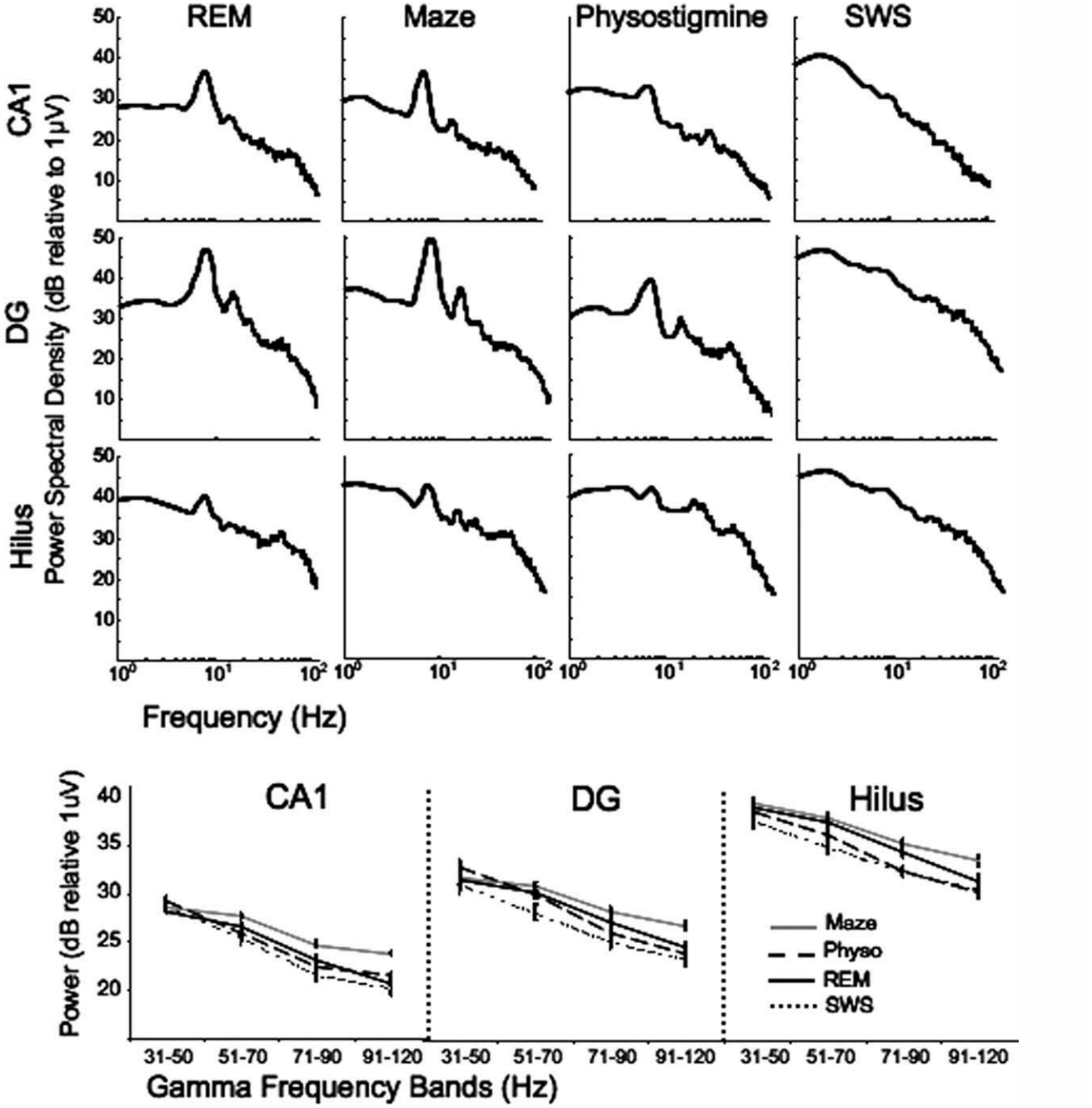

FIGURE 2. A: Exemplar power spectral density plots for maze running, REM sleep, physostigmine, and slow wave sleep conditions. Note power in theta band during SWS. Power is presented in decibels relative to 1 μV. Frequency is presented on a log scale. B: Average gamma power for maze running, REM sleep, physositgmine, and slow wave sleep conditions. Power is calculated for 20 Hz frequency bands. Gamma power was significantly higher during maze running for the highest frequency band (91–120 Hz, $P < 0.01$). All state comparisons were made for homotopic (ispilaerally) and homotypic (contralaterally) laminar and areal positions.

quartile comparison). Further, there was a very high positive correlation between the normalized coherence and standard coherence, with an $r = 0.99$ for REM, $r = 0.98$ for the maze condition, $r = 0.97$ following physostigmine treatment, and $r = 0.98$ during SWS. For these reasons we considered the normalized coherence a more conservative estimate of the coherence and thus used normalized coherence for all of our subsequent analyses (see Sabolek et al., 2009; Hinman et al., 2011). For completeness, we also report coherence across hemispheres between all quartiles and the septal contralateral quartile (see Fig. 3). In agreement with our prior report (Sabolek et al., 2009), the coherence of theta decreased significantly between homotopic (e.g., CA1 to CA1; DG to DG) sites located across quartile boundaries for CA1, DG and hilus sites (P's <0.05; compare panels B, C, and D or E, F, and G). In contrast, coherence among homotypic sites across hemispheres

TABLE 3.

Theta and Gamma Power Ratios

	CA1	DG	Hilus
Theta (6–10 Hz)/wide band (1–100 Hz) power ratio			
Maze running	0.95 ± 0.003	0.94 ± 0.007	0.86 ± 0.005[a]
REM	0.95 ± 0.004	0.94 ± 0.006	0.87 ± 0.005[a]
Physostigmine	0.91 ± 0.009[b]	0.92 ± 0.010[b]	0.84 ± 0.007[a,b]
SWS	0.83 ± 0.003[c]	0.85 ± 0.005[c]	0.85 ± 0.003[c]
Gamma (40–100 Hz)/wide band (1–100 Hz) power ratio			
Maze running	0.73 ± 0.005	0.76 ± 0.008[e]	0.85 ± 0.005[d]
REM	0.71 ± 0.007	0.75 ± 0.006[e]	0.86 ± 0.006[d]
Physostigmine	0.74 ± 0.008[g]	0.77 ± 0.008[e,g]	0.85 ± 0.005[d]
SWS	0.65 ± 0.010[f]	0.69 ± 0.008[f]	0.78 ± 0.007[f]

All values expressed as dB relative to 1 μV in theta band (6–10 Hz) divided by dB relative to 1 μV across wide band (1–100 Hz).All values expressed as dB relative to 1 μV in gamma band (40–100 Hz) divided by dB relative to 1 μV across wide band (1–100 Hz).

[a]Hilar sites had a significantly lower power ratio ($P < 0.001$) when compared to CA1 and DG sites across all theta states.

[b]All sites had a significantly lower power ($P < 0.01$) following physostigmine compared with during maze running and REM.

[c]All sites had a significantly lower power ratio ($P < 0.01$) during SWS as compared with maze running and REM.

[d]Hilar sites had a significantly higher power ratio ($P < 0.001$) when compared with CA1 and DG sites across all theta states.

[e]DG sites had a significantly higher power ratio ($P < 0.001$) when compared with CA1 sites across all theta states.

[f]All sites exhibited a significantly lower power ratio ($P < 0.001$) during SWS.

[g]There was a significant increase in the power ratio ($P < 0.01$) following physostigmine in CA1 and DG.

(e.g., Fig. 3A a–c,) within the septal hippocampus was not different from coherence among sites within the first quartile in the same hemisphere (compare Figs. 3B and 4E).

Theta Coherence Across Different Behavioral States

Our main hypothesis was that theta coherence would increase across the septotemporal axis during awake locomotor activity reflecting increased dominance of EC inputs and the general excitatory (depolarizing) influences of subcortical modulatory (e.g., cholinergic) inputs. However, we observed no significant differences in theta coherence across the septotemporal axis during maze running as compared to REM sleep. Specifically, for any group of homotopic electrode pairs (e.g., CA1 to CA1 within hemisphere within the first quartile, or across the first and second quartiles; see Figs. 3B and 4C), no significant differences were observed (P's > 0.1) across θ-associated behavioral states (running, REM), although theta coherence in the DG tended to be lower during physostigmine treatment as compared to maze running.

There were obvious decreases in theta coherence during SWS at all CA1-CA1 and DG-DG pairs, while the decrease in coherence across hilar-hilar pairs was quite variable. On this note, we report that the decrease in theta coherence across the long axis is quite evident during SWS where there is a roughly 50% decrease across each successive quartile (P's < 0.001; see Fig. 3 comparing Panels B, C, and D). The decrease in theta coherence observed during SWS is much greater than that observed during θ-associated states, diminishing to values less than 0.1 at the most septotemporal distances (see Figs. 3D and 3G). Note that these values are expressed as normalized coherence, so that coherence across distant septotemporal electrodes during SWS in the theta band is still greater than one would expect by chance.

Gamma Coherence and θ-γ Cross-Frequency Coupling

Gamma coherence decreases much more rapidly with distance than theta coherence with more than a 60% decrease in coherence beyond roughly 1 mm distances (see Sabolek et al., 2009). The majority of our electrodes were positioned beyond 1–2 mm distances within the ipsilateral hemisphere, which are distances that typically yield gamma coherence values between 0.0–0.3 (see Sabolek et al., 2009). While there was an obvious decrease in coherence across quartile distances (see Table 4), no theta state dependent differences were observed (see Table 4 or Fig. 4A). Gamma coherence was significantly lower during SWS for homotopic CA1-CA1, but not across homotopic DG-DG or hilar sites (see Fig. 4A).

We also examined the modulation of gamma by theta and demonstrate that cross frequency coupling is reduced at DG sites during physostigmine-induced theta compared with maze running and REM sleep (see Fig. 4B, $P < 0.01$). No change in the θ-γ relationship was observed at either CA1 or hilar sites. Table 5 illustrates cross-frequency coupling coherence for all electrode positions at each quartile of the hippocampus.

DISCUSSION

Our main hypothesis was that theta coherence would increase across the septotemporal axis during locomotor activity as compared to REM sleep. However, we observed no significant differences in theta coherence across the septotemporal axis during maze running, REM sleep or physostigmine-induced theta. This was true between sites that exhibited quite high coherence (e.g., 0.7–0.9 between sites within the same septotemporal quartile of the HPC and across homotypic sites in the contralateral hemispheres). This was also true between sites more distant across the septotemporal axis that exhibited relatively low coherence values (0.2–0.5). Thus, our first main finding is that the general pattern of theta coherence across the septotemporal axis is unchanged across distinct θ-associated behavioral states (locomotion, REM sleep and cholinesterase induced theta during immobility). These findings demonstrate that the general pattern of theta coherence across the septotemporal axis, while varying systematically (decreasing), does not

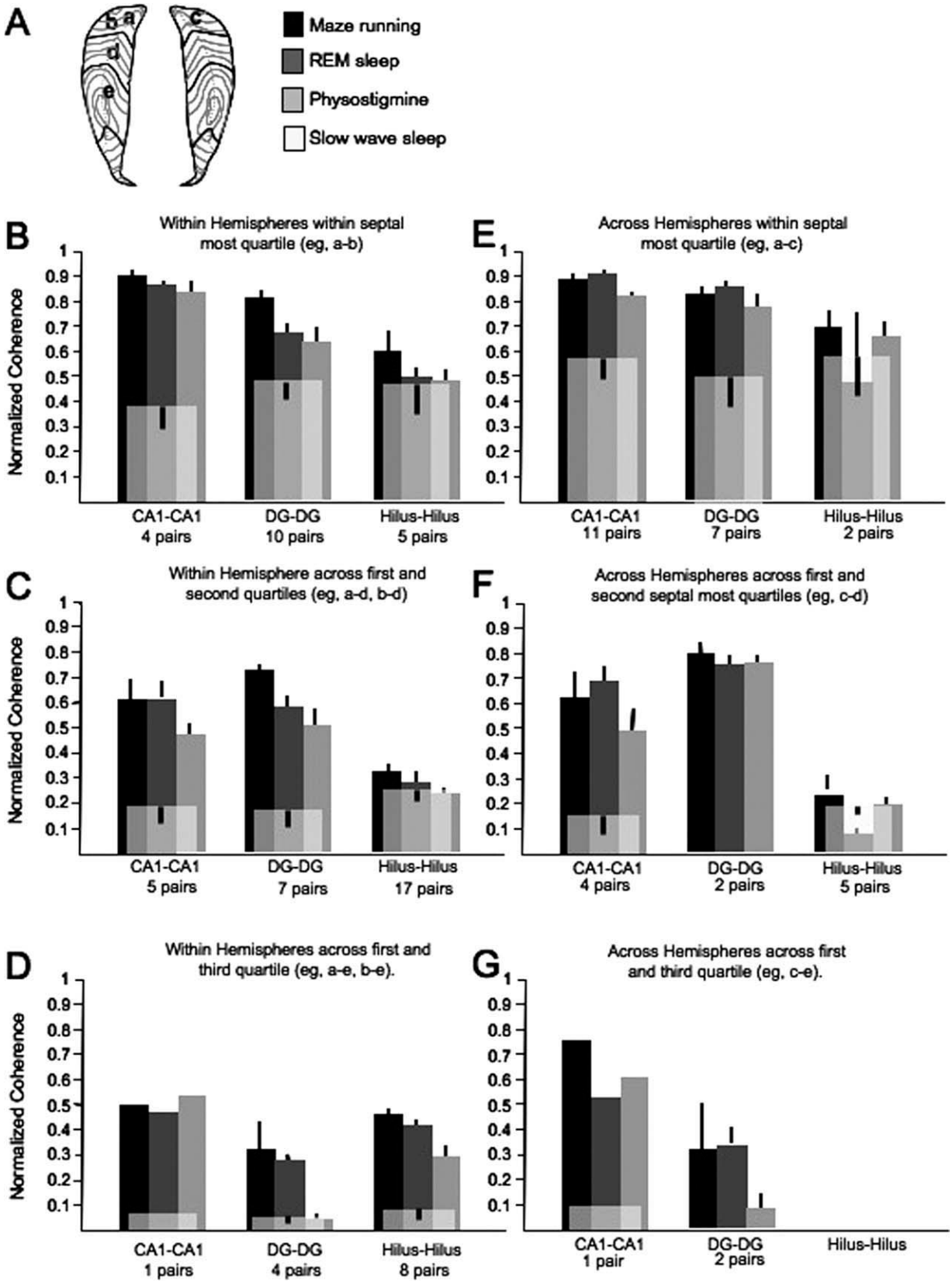

FIGURE 3. Theta coherence of homotopic (ispilaerally) and homotypic (contralaterally) recording locations along the areal extent of the hippocampus. A: A flatmap representation of the dentate gyrus (both hemispheres). The hippocampal sub regions have been divided into quartiles. B–D: Columns signify ipsilateral homotopic recording locations. The first column indicates the coherence of two signals recorded within the CA1 sub region, in the second column recordings in the DG, and in the third column recordings in the hilus. Rows were segregated by the relationship of the areal position of the two recording sites. So the coherence values in the first row were from electrodes positioned within the same 25% of the hippocampus (i.e., a–b). The second row represents the coherence between adjacent quartiles (i.e., a–d, b–d), and the third row indicates coherence when recording sites were separated by at least 25% of the hippocampus (i.e., a–e). E-G) Columns signify contralateral, homotypic recording locations.

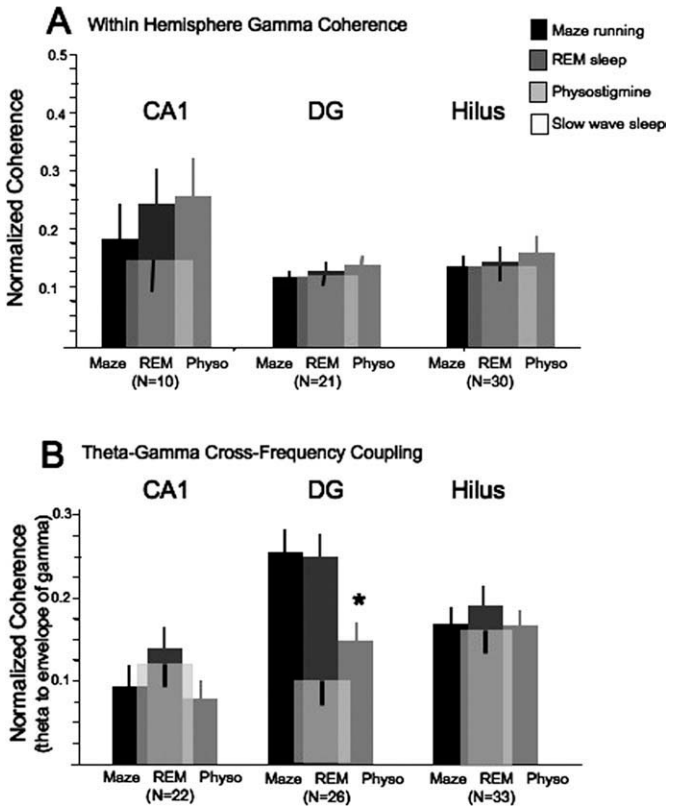

FIGURE 4. A: Gamma coherence of homotopic recording locations within the ipsilateral CA1, DG, and hilar subfields during maze running, REM sleep, physostigmine treatment and slow wave sleep. B: The cross-frequency coupling of theta and gamma during maze running, REM sleep, physostigmine, and SWS conditions. Coherence values are calculated within electrode, for homotopic recording locations.

change in relation to gross changes in sensory input or overt behavior.

Second, the present findings highlight that the decrease in theta coherence along the septotemporal axis observed during REM sleep (Sabolek et al., 2009) is also evident during locomotion across a maze, as well as during physostigmine-induced theta (awake-immobility). Third, we report that theta modulation of gamma at all sites is similar during locomotor activity and REM sleep; however, the coupling of theta to gamma was significantly reduced during physostigmine-induced theta in both CA1 and the DG.

Why One Might Expect Differences in Theta/Gamma as a Function of State

There are two major populations of glutamateric excitatory afferents that are critical to theta current generation. First, the CA3/mossy cell afferents innervating CA1 and DG, respectively and the Layers 2 and 3 entorhinal afferents that innervate CA1 and DG, respectively. There is a large difference in the topographic distribution of these afferents along the septotemporal axis. CA3 neurons and related mossy cells project extensively along the long axis and across hemispheres in the rodent (Ishizuka et al., 1990; Li et al., 1994; Amaral and Witter, 1995). In contrast, unilateral entorhinal afferents define three areal zones along the septotemporal axis with the largest area zone, the septal 50%, receiving input from a narrow lateral band of entorhinal neurons near the rhinal sulcus (Dolorfo and Amaral, 1998). Additionally, there is septotemporal variation in the density and topography of subcortical modulatory inputs (e.g., Gage and Thompson, 1980; Amaral and Kurz, 1985; see also Thompson et al., 2008 for an excellent review).

Our simple hypothesis was that variation in the contribution of these two afferent (CA3 and EC) projections (e.g., Ang et al., 2005), as well as widespread changes in the activity of subcortical afferents (e.g., Brown et al., 2005) would be reflected in changes in theta coherence. While the current findings illustrate clear decreases in theta coherence along the septotemporal axis during REM, maze running, as well as physostigmine-induced theta, no differences were observed between these distinct theta states despite quite widespread difference in the behavior of the animal.

In this regard, one might conclude that theta coherence across the septotemporal axis reflects a fairly fixed anatomical substrate. A few studies have indicated significant changes in theta and gamma coherence across laminar-specific sites in the septal HPC as a function of state and information processing (see Montgomery et al., 2008, 2009; see also Jones and Wilson, 2005; Kay, 2005 and Martin, Beshel and Kay, 2007). Similarly, a number of human and animal studies have demonstrated a relationship between theta power and coherence, as well as gamma and theta/gamma coupling at both medial temporal lobe and other neocortical sites in relation to information processing (e.g., Fell

TABLE 4.

Gamma Coherence by Distance

	CA1-CA1	DG-DG	Hilus-Hilus
Within hemisphere first septal quartile			
	(N = 4)	(N = 10)	(N = 5)
Maze running	0.30 ± 0.14	0.15 ± 0.02	0.18 ± 0.09
REM	0.38 ± 0.11	0.17 ± 0.02	0.27 ± 0.15
Physostigmine	0.37 ± 0.14	0.18 ± 0.03	0.24 ± 0.17
SWS	0.26 ± 0.13	0.16 ± 0.03	0.25 ± 0.15
Within hemisphere first to second quartile			
	(N = 5)	(N = 7)	(N = 17)
Maze running	0.11 ± 0.02	0.11 ± 0.01	0.14 ± 0.02
REM	0.17 ± 0.05	0.11 ± 0.01	0.14 ± 0.02
Physostigmine	0.19 ± 0.05	0.11 ± 0.01	0.17 ± 0.02
SWS	0.08 ± 0.01	0.08 ± 0.01	0.12 ± 0.01
Within hemisphere first to third quartile			
	(N = 1)	(N = 4)	(N = 8)
Maze running	0.10 ± N/A	0.07 ± 0.01	0.11 ± 0.01
REM	0.08 ± N/A	0.07 ± 0.02	0.08 ± 0.02
Physostigmine	0.14 ± N/A	0.09 ± 0.04	0.11 ± 0.01
SWS	0.06 ± N/A	0.10 ± 0.02	0.11 ± 0.01

All values expressed as normalized coherence ± SEM. Values are averaged across homotopic (e.g., CA1-CA1) and septo-temporal positions. *N*, number of homotopic electrode pairs.

TABLE 5.

Cross Frequency Coupling by Distance

	CA1	DG	Hilus
First quartile			
	(N = 16)	(N = 17)	(N = 12)
Maze running	0.07 ± 0.03	0.22 ± 0.03	0.16 ± 0.03
REM	0.14 ± 0.03	0.26 ± 0.03	0.12 ± 0.03
Physostigmine	0.04 ± 0.01	0.18 ± 0.02	0.15 ± 0.02
SWS	0.13 ± 0.02	0.09 ± 0.02	0.13 ± 0.03
Second quartile			
	(N = 3)	(N = 7)	(N = 14)
Maze running	0.15 ± 0.08	0.29 ± 0.08	0.13 ± 0.02
REM	0.17 ± 0.10	0.24 ± 0.08	0.18 ± 0.04
Physostigmine	0.13 ± 0.06	0.08 ± 0.04	0.19 ± 0.04
SWS	0.08 ± 0.04	0.12 ± 0.04	0.17 ± 0.04
Third quartile			
	(N = 3)	(N = 2)	(N = 7)
Maze running	0.13 ± 0.11	0.41 ± 0.14	0.11 ± 0.01
REM	0.09 ± 0.04	0.23 ± 0.05	0.08 ± 0.02
Physostigmine	0.24 ± 0.10	0.09 ± 0.04	0.11 ± 0.01
SWS	0.14 ± 0.03	0.06 ± 0.02	0.11 ± 0.01

All values expressed as normalized coherence ± SEM.

et al., 2001, 2003; Sederberg et al., 2003; Canolty et al., 2006; Shirvalkar et al., 2009; Tort et al., 2010). In contrast to these studies, our interest has focused on global alterations in theta and/or gamma indices across the septotemporal axis as a means to examine the relationship between these physiological indices, topographic anatomy (e.g., Dolorfo and Amaral, 1998) and functional differentiation across the long axis. Surprisingly, the present data demonstrate that the decrease in theta coherence across the septotemporal axis was not notably different during running or immobility related to physostigmine treatment. In many respects, the absence of differences in theta coherence is reminiscent of early neuroimaging studies where novel and trial-unique stimuli were required to evidence BOLD signal activation of HPC and anterior-posterior differences in HPC response to particular stimuli (see Strange et al., 1999 or Hasselmo and Stern, 2006 or Strange and Dolan, 2006 for reviews). Our recent findings also indicate that environmental novelty produces significant change in theta coherence across the septoemporal axis, as well as between hippocampal and entorhinal cortical sites (Penley, unpublished observations). Thus, it appears that theta coherence exhibits considerable variation along the septotemporal axis at both CA1 and DG sites and that dynamic variability in theta signals may offer insight into stimuli and information processing states that engage HPC processing.

SUMMARY

Considerable information is available about the discharge characteristics of hippocampal neuronal populations (e.g., CA1 pyramidal, CA3 pyramidal, granule cells and interneurons), as well as any number of subcortical and necortical neurons in relation to theta field potentials. Theta and other frequency rhythms support the temporal organization of neuronal discharge, a mechanism to create temporally organized ensembles. We suspect that greater (or less) coherence of LFP signals across sites within the HPC could reflect more temporally precise synaptic inputs (or less) impinging on the dendritic fields in the vicinity of the recording sites. Thus, greater coherence reflecting a larger, more synchronous, neuronal circuit engaged in emergent function (e.g., encoding patterns of entorhinal input related to ongoing sensory events). Alternately, less coherence between sites could represent less temporally precise synaptic input perhaps as a consequence of temporal segregation of synaptic inputs from EC inputs. Our goal has been to describe the general pattern of theta coherence, as an index of functional interaction between sites across the septotemporal axis. The present findings illustrate that there is considerable difference in theta coherence across the septotemporal axis that is not particularly sensitive to gross differences in locomotor behavior (same during running as during REM sleep). Further studies will be required to characterize the environmental conditions (e.g., novelty) or information-processing state (e.g., encoding, retrieval) that produce alterations in theta coherence, gamma coherence or for that matter alterations of θ-γ cross-frequency coupling along the septotemporal axis of the HPC.

Acknowledgments

Histological assistance from University of Connecticut undergraduate students Jeremy Friel and Lauren Long.

REFERENCES

Alonso A, Garcia-Austt E. 1987. Neuronal sources of theta rhythm in the entorhinal cortex of the rat. II. Phase relations between unit discharges and theta field potentials. Exp Brain Res 67:502–509.

Amaral DG, Kurz J. 1985. An analysis of the origins of the cholinergic and noncholinergic septal projectiotions to the hippocampal formation of the rat. J Comp Neurol 240:37–59.

Amaral DG, Witter MP. 1995. The three-dimensional organization of the hippocampal formation: A review of anatomical data. Neuroscience 31:371–391.

Ang CW, Carlson GC, Coulter DA. 2005. Hippocampal CA1 circuitry dynamically gates direct cortical inputs preferentially at theta frequencies. J Neurosci 25:9567–9580.

Aston-Jones G, Bloom FE. 1981. Activity of norepinephrine-containing locus coeruleus neurons in behaving rats anticipates fluctuations in the sleep-waking cycle. J Neurosci 1:876–886.

Bannerman DM, Rawlins JN, McHugh SB, Deacon RM, Yee BK, Bast T, Zhang WN, Pothuizen HH, Felton J. 2004. Regional dissociations with the hippocampus-memory and anxiety. Neurosci Biobehav Rev 28:273–283.

Bland BH. 1986. Physiology and pharmacology of hippocampal formation theta rhythms. Prog in Neurobiology 26:1–54.

Bland BH, Oddie standarddeviation (SD). 2001. Theta band oscillation and synchrony in the hippocampal formation and associated

structures: The case for its role in sensorimotor integration. Behav Brain Res 127:119–136.
Borthegyi Z, Varga V, Szilagyi N, Fabo D, Freund TF. 2004. Phase segregation of medial septal GABAergic neurons during hippocampal theta activity. J Neurosci 29:8470–8479.
Bragin A, Jando G, Nadasdy Z, Hetke J, Wise K, Buzsaki G. 1995. Gamma (40–100 Hz) oscillation in the hippocampus of the behaving rat. J Neurosci 15:47–60.
Brankack AJ, Stewart M, Fox SE. 1993. Current source density analysis of the hippocampal theta rhythm: Associated sustained potentials and candidate synaptic generators. Brain Res 615:310–327.
Brazhnik ES, Fox SE. 1999. Action potentials and relations to the theta rhythm of medial septal neurons in vivo. Exp Brain Res 127:244–258.
Brown RA, Walling SG, Milway JS, Harley CW. 2005 Locus ceruleus activation suppresses feedforward interneurons and reduces beta-gamma electroencephalogram frequencies while it enhances theta frequencies in rat dentate gyrus. J Neurosci 2005; 25:1985–1991.
Bullock TH, Buzsaki G, McClune MC. 1990. Coherence of compound field potentials reveals discontinuities in the CA1-subiculum of the hippocampus of the freely-moving rat. Neuroscience 38:609–619.
Buzsaki G, Leung L, Vanderwolf CH. 1983. Cellular basis of hippocampal EEG in the behaving rat. Brain Res Rev 6:139–171.
Buzsaki G, Chrobak JJ. 1995. Temporal structure in spatially organized neuronal ensembles: A role for interneuronal networks. Curr Opin Neurobiol 5:504–510.
Buzsaki G. 2002. Theta oscillations in the hippocampus. Neuron 33:325–340.
Canolty RT, Edwards E, Dalal SS, Soltani M, Nagarajan SS, Kirsch HE, Berger MS, Barbaro NM, Knight RT. 2006. High gamma power is phase-locked to theta oscillations in human neocortex. Science 313:1626–1628.
Chrobak JJ, Buzsaki G. 1998. Gamma oscillations in the entorhinal cortex of the freely behaving rat. J Neurosci 18:388–398.
Csicsvari J, Jamieson B, Wise KD, Buzsaki G. 2003. Mechanisms of gamma oscillations of the behaving rat. Neuron 37:311–322.
Dolorfo C, Amaral DG. 1998. Entorhinal cortex of the rat: Topographic organization of the cells of origin of the perforant path projections to the dentate gyrus. J Comp Neurol 398:25–48.
Efron B, Tibshirani RJ. 1993. An Introduction to the Bootstrap. New York: Chapman & Hall.
Fell J, Klaver P, Lehnertz K, Grunwald T, Schaller C, Egler CE, Fernandez G. 2001. Human memory formation is accompanied by rhinal-hippocampal coupling and decoupling. Nat Neurosci 4:1259–1264.
Fell J, Klaver P, Elfadil H, Schaller C, Elger CE, Fernandez G. 2003. Rhinal-hippocampal theta coherence during declarative memory formation: Interaction with gamma synchronization. EJ Neurosci 17:1082–1088.
Freund TF, Antal M. 1988. GABA-containing neurons in the septum control inhibitory interneurons in the hippocampus. Nature 336:170–173.
Gage FH, Thompson RG. 1980. Differential distribution of norepinephrine and serotonin along the dorsal-ventral axis of the hippocampal formation. Brain Res Bull 5:771–773.
Gray CM. 1994. Synchronous oscillations in neuronal systems: Mechanisms and functions. Com Neurosci 1:11–38.
Hajos N, Palhalmi J, Mann EO, Nemath B, Paulsen O, Freund TF. 2004. Spike timing of distinct types of GABAergic interneurons during hippocampal gamma oscillations in vitro. J Neurosci 24:9127–9137.
Hangya B, Borhegyi Z, Szilagyi N, Freund TF, Varga V. 2009. GABAergic neurons of the medial septum lead the hippocampal network during theta activity. J Neurosci 24:8094–8102.
Harley CW. 2007. Norepinephrine and the dentate gyrus. Prog Brain Res 163:299–318.
Hasselmo ME. 2006. The role of ACh in learning and memory. Curr Opin Neurobiol 15:710–715.
Hasselmo ME, Stern CE. 2006. Mechanisms underlying working memory for novel information. Trends Cogn Sci 10:487–493.
Hentschke H, Perkins MG, Pearce RA, Banks MI. 2007. Muscarinic blockade weakens interaction of gamma with theta rhythms in mouse hippocampus. Eur J Neurosci 26:1642–1656.
Hinman JR, Penley SC, Long LL, Escabi MA, Chrobak JJ. 2011. Septotemporal variation in dynamics of theta: speed and habituation. J Neurophysiol 105:2675–2686.
Ishizuka N, Weber J, Amaral DG. 1990. Organization of intrahippocampal projections from CA3 pyramidal cells in the rat. J Comp Neurol 295:580–623.
Jones MW, Wilson MA. 2005. Theta rhytms coordinate hippocampal-prefrontal interactions in a spatial memory task. PLOS Biol 3:402.
Kametani H, Kawamura H. 1990. Alterations in ACh release in the rat hippocampus during sleep-wakefulness detected by intracerebral dialysis. Life Sci 47:421–426.
Kay LM. 2005. Theta oscillations and sensorimotor performance. Proc Natl Acad Sci USA 102:3863–3868.
Kocsis B, Thinschmidt JS, Kinney GG, Vertes RP. 1994. Seperation of hippocampal theta dipoles by partial coherence analysis in the rat. Brain Res 660:341–345.
Konopacki J, Bland BH, Colom LV, Oddie SD. 1992. In vivo intracellular correlates of hippocampal formation theta-on and theta-of cells. Brain Res 586:247–255.
Kramis R, Vanderwolf CH, Bland BH. 1975. Two types of hippocampal rhythmical slow activity in both the rabbit and the rat: relations to behavior and effects of atropine, diethyl ether urethane, and pentobarbital. Expl Neural 49:58–85.
Knierim JJ, Lee I, Hargreaves EL. 2006. Hippocampal place cells: parallel input stream, subregional processing and implications for episodic memory. Hippocampus 16:755–764.
Lee MG, Chrobak JJ, Sik A, Wiley RG, Buzsaki G. 1994. Hippocampal theta activity following selective lesion. Neuroscience 62:1033–1047.
Leung LS, Vanderwolf CH. 1980. Behavior-dependent evoked potentials in the hippocampal CA1 region of the rat. II. Effect of eserine, atropine, ether and pentobarbital. Brain Res 198:119–133.
Leung LW, Buzsáki G. 1983. Spectral analysis of hippocampal unit train in relation to hippocampal EEG. Electroencephalogr Clin Neurophysiol 56:668–671.
Leung LS. 1985. Spectral analysis of hippocampal EEG in the freely moving rat: Effects of centrally active drugs and relation to evoked potentials. Electroencephalogr Clin Neurophysiol 60:65–77.
Leung L-WS. 1984. Theta rhythm during REM sleep and waking: Correlations between power, phase and frequency. Electroencephalogr Clin Neurophysiol 58:553–564.
Llinas R, Grace AA, Yarom Y. 1991. In vitro neurons in mammalian cortical layer 4 exhibit intrinsic oscillatory activity in the 10- to 50-Hz frequency range. Proc Natl Acad Sci USA 88:897–901.
Llinas R, Urbano FJ, Leznik E, Ramirez RR, van Marle HJ. 2005. Rhythmic and dysrhythmic thalamocortical dynamics: GABA systems and the edge effect. Trends Neurosci 28:325–333.
Li XG, Somogyi P, Ylinen A, Buzsaki G. 1994. The hippocampal CA3 network: an in vivo intracellular labeling study. J Comp Neurol 339:181–208.
Manseau F, Goutagny R, Danik M, Williams S. 2008. The hippocamposeptal pathway generates rhythmic firing of GABAergic neurons in the medial septum and diagonal bands: An investigation using a complete septohippocampal preparation in vitro. J Neurosci 28:4096–4107.
Marrosu F, Portas C, Mascia MS, Casu MA, Fa M, Giagheddu M, Imperato A, Gessa GL. 1995. Microdialysis measurement of cortical and hippocampal ACh release during sleep-wake cycle in freely moving cats. Brain Res 671:329–332.

Montgomery SM, Sirota A, Buzsaki G. 2008. Theta and gamma coordination of hippocampal networks during waking and rapid eye movement sleep. J Neurosci 28:6731–6741.

Moser MB, Moser EI. 1998. Functional differentiation in the hippocampus. Hippocampus 8:608–619.

O'Keefe J, Recce ML. 1993. Phase relationship between hippocampal place units and the EEG theta rhythm. Hippocampus 3:317–330.

Roark RM, Escabi MA. (1999). B-spline design of maximally flat and prolate spheroidal-type FIR filters. IEEE Trans Signal Proc 47:701–716.

Royer S, Sirota A, Patel J, Buzsaki G. 2010. Distinct representations and theta dynamics in dorsal and ventral hippocampus. J Neurosci 30:1777–1787.

Sabolek HR, Penley SC, Hinman JR, Bunce JG, Markus EJ, Escabi M, Chrobak JJ. 2009. Theta and gamma coherence along the septotemporal axis of the hippocampus. J Neurophysiol 101:1192–1200.

Sederberg PB, Kahana MJ, Howard MW, Donner EJ, Madsen JR. 2003. Theta and gamma oscillations during encoding predict subsequent recall. J Neurosci 23:10809–10814.

Shirvalkar PR, Rapp PR, Shapiro ML. 2010. Bidirectional changes to hippocampal theta-gamma comodulation predict memory for recent spatial episodes. Proc Natl Acad Sci USA 107:7054–7059.

Sil'kis IG. 2009. Characteristics of the functioning of the hippocampal formation in waking and paradoxical sleep. Neurosci Behav Physiol 39:261–275.

Strange BA, Fletcher PC, Henson RN, Friston KJ, Dolan RJ. 1999. Segregating the functions of the human hippocampus. Proc Natl Acad Sci USA 96:4034–4039.

Strange BA, Dolan RJ. 2006. Anterior medial temporal lobe in human cognition: memory for fear and the unexpected. Cogn Neuropsychiatry 11:198–218.

Swanson LW, Wyss JM, Cowan WM. 1978. An autoradiographic study of the organization of intrahippocampal association pathways in the rat. J Comp Neurol 181:681–715.

Thompson CL, Pathak SK, Jeromin A, Ng LL, MacPherson CR, Mortrud MT, Cusick A, Riley ZL, Sunkin SM, Bernard A, Puchalski RB, Gage FH, Jones AR, Bajic VB, Hawrylycz MJ, Lein ES. 2008. Genomic anatomy of the hippocampus. Neuron 26:1010–1021.

Toth K, Borhegyi Z, Freund TF. 1993. Postsynaptic targets of GABAergic hippocampal neurons in the medial septum-diagonal band of Broca complex. J Neurosci 13:3712–3724.

Tort AB, Komorowski RW, Manns JR, Kopell NJ, Eichenbaum H. 2009. Theta-gamma coupling increases during the learning of item-context associations. Proc Natl Acad Sci USA 106:20942–20947.

Trulson ME, Trulson VM. 1982. Activity of nucleus raphe pallidus neurons across the sleep-waking cycle in freely moving cats. Brain Res 8; 237:232–237.

Vertes RP, Kocsis B. 1997. Brainstem-diencephalo-septohippocampal systems controlling the theta rhythm of the hippocampus. Neuroscience 81:893–926.

Welch PD. 1967. The use of fast fourier transform fot he estimation of power spectra: A method based on time averaging over short, modified periodograms. IEEE Trans Audio Electroacoust 15:70–73.

Ylinen A, Soltesz I, Bragin A, Penttonen M, Sik A, Buzsaki G. 1995. Intracellular correlates of hippocampal theta rhythm in identified pyramidal cells, granule cells, and basket cells. Hippocampus 5:78–90.